D7.10 New measurement and modelling methodologies for high resolution monitoring of urban anthropogenic and biogenic CO2 fluxes

Konstantinos Politakos

Emmanouil Panagiotakis

Stavros Stagakis

Nektarios Chrysoulakis

CoCO2
Prototype system for a
Copernicus CO$_2$ service

D7.10 New measurement and modelling methodologies for high resolution monitoring of urban anthropogenic and biogenic CO₂ fluxes

Dissemination Level:	Public
Author(s):	Konstantinos Politakos (FORTH)
	Stavros Stagakis (FORTH)
	Emmanouil Panagiotakis (FORTH)
	Nektarios Chrysoulakis (FORTH)
Date:	22/10/2023
Version:	0.2
Contractual Delivery Date:	31/09/2023
Work Package/ Task:	WP7/ T7.5
Document Owner:	FORTH
Contributors:	CICERO, BSC
Status:	Final

CoCO2: Prototype system for a Copernicus CO₂ service

Coordination and Support Action (CSA)
H2020-IBA-SPACE-CHE2-2019 Copernicus evolution –
Research activities in support of a European operational
monitoring support capacity for fossil CO2 emissions

Project Coordinator: Dr Richard Engelen (ECMWF)
Project Start Date: 01/01/2021
Project Duration: 36 months

Published by the CoCO2 Consortium

Contact:
ECMWF, Shinfield Park, Reading, RG2 9AX,
richard.engelen@ecmwf.int

Table of Contents

Figures

Tables

1 Executive Summary

The primary objective of this report is to integrate various observation systems with dynamic datasets and advanced high-resolution modelling systems. This integration aims to effectively capture the spatiotemporal variations in CO_2 concentrations and flux distributions within urban environments. Consequently, this approach enhances our ability to distinguish and differentiate between anthropogenic and biogenic CO_2 fluxes, contributing to a deeper understanding of urban carbon dynamics.

The work described in this report is separated into two locations (Heraklion and Basel) where urban flux towers have been active since several years. In order to assess the urban fluxes at the two cities, two different urban flux models (SUEWS, diFUME) have been applied (one at each city) and the model estimations are compared to the urban flux observations from the available towers. In addition to the urban flux datasets from the towers, a series of other datasets are used in the modelling process, such as remote sensing imagery, meteorological observations, population and traffic data.

This report demonstrates the complexity of the urban CO_2 flux spatiotemporal dynamics and the need of the combined use of models and in-situ observations to achieve a thorough assessment of the main processes contributing to the total emissions originating from urban areas.

2 Introduction

2.1 Background

In recent decades, the global scientific community has set an aim of advancing the CO_2 monitoring estimates, with a concurrent focus on initiatives and commitments, e.g. the Paris Agreement, geared towards addressing the escalating rate of CO_2 concentrations. In this direction, numerous endeavours have been received, and a compendium of methodologies has been assembled monitoring the environment via satellites e.g. the (OCO-2) satellite by NASA, or additionally the Greenhouse Gases Observing Satellite (GOSAT), run by Japan. Pioneering research is focused on assessing the efficacy of atmospheric models in computing and estimating carbon dioxide emissions at finer spatial resolutions. Through the Copernicus effort, the European Union in particular has developed monitoring and estimation models of CO_2 in order to produce and make data accessible for more research and study. Within this context, forthcoming years will witness the launch of CO2MVS, a comprehensive initiative aimed at enhancing the precision of spatial and temporal CO_2 estimations, which will leverage state-of-the-art inversion techniques, allowing for continuous monitoring of emissions and tracking of temporal and spatial alterations, aiming at both natural physical processes and anthropogenic sources (e.g. combustion of fossil fuels).

Conversely, researchers are actively engaged in the direct measurement of heat and CO_2 emissions, encompassing diverse geographic dimensions. This approach presents a unique opportunity as it allows for precise examination of various environments across extensive temporal and spatial scales, which, until now, is unattainable through satellite imaging.

2.2 Scope of this deliverable

2.2.1 Objectives of this deliverable

This demonstrator will showcase outcomes derived from urban ecosystem models focusing on spatiotemporal CO_2 flux profiles within the urban environment in fine scales. The datasets employed consist of in-situ urban eddy covariance measurements from two urban case studies

D7.10 New measurement and modelling methodologies for high resolution monitoring of urban anthropogenic and biogenic CO_2 fluxes

Heraklion, Greece and Basel, Switzerland, in additional to satellite images, meteorological and human activity input.

2.2.2 Work performed in this deliverable

The Surface Urban Energy and Water Balance Scheme (SUEWS) is used in Heraklion's datasets (Ward et al., 2016) and a new high-resolution modeling approach of urban CO$_2$ fluxes called diFUME (Stagakis, Feigenwinter, Vogt, & Kalberer, 2023) for Basel's.

2.2.3 Deviations and counter measures

The Heraklion datasets used in this presentation relate to the years 2019 for TomTom data, 2020 for traffic counts, and 2018 for flux tower measurements. This is because COVID-19 limitations have influenced residential mobility patterns and lowered traffic flows.

3 SUEWS Model

3.1 Model description

The Surface Urban Energy and Water balance Scheme (hereinafter: SUEWS) is used to simulate energy, water and CO2 fluxes (L. Järvi et al., 2011). The model is centered on the urban energy balance (Oke, 1987),

$$Q* + Q_F = Q_H + Q_E + \Delta Q_S \qquad \textbf{(1)}$$

and urban water balance (Grimmond et al., 1986),

$$P + I_e = E + R + \Delta S \qquad \textbf{(2)}$$

where $Q*$ is the net all-wave radiation, Q_F the anthropogenic heat flux, Q_H the turbulent sensible heat flux, Q_E the latent heat flux and ΔQ_S the net storage heat flux; P is precipitation, I_e the water supplied by irrigation or street cleaning, E the evaporation, R the runoff (including above-ground runoff and deep soil runoff) and ΔS the net change in water storage (including water in the soil and water held on the surface).

SUEWS has recently been advanced to include a CO$_2$ flux module, that adopts a bottom-up approach to determine the local-scale CO$_2$ flux:

$$F_C = F_M + F_V + F_B + F_P + F_{pho} + F_{res} \qquad \textbf{(3)}$$

The CO$_2$ module allows for a partitioning of the CO$_2$ fluxes into its anthropogenic: human metabolism (F_M), traffic (F_V), buildings (F_B), and from local-scale point sources (F_P), and biogenic components: photosynthetic uptake (F_{pho}) and ecosystem respiration (F_{res}). F_{pho} is modeled with the empirical canopy model, which accounts for responses of plant stomatal control on environmental conditions. CO$_2$ flux from soil and plant respiration's (F_{res}) is modeled as exponentially depending on air temperature.

The evaluation of the SUEWS model has been conducted in two urban areas within the United Kingdom, yielding crucial insights into the urban functionality among diverse urban sites and potential future modifications (Ward et al., 2016). Furthermore, The evaluation of the SUEWS on CO$_2$ fluxes has been studied in Helsinki and Beijing (Leena Järvi et al., 2019; Zheng et al., 2023). Both studies employed eddy covariance measurements from nearby flux towers to investigate anthropogenic and biogenic emissions in urban environments. Moreover, the model serves as a valuable tool for assessing various urban planning scenarios (Panagiotakis et al., 2021), particularly in estimating carbon emissions at the local scale before implementing policy measures.

3.2   Model Input

3.2.1   Flux Observations and Meteorological data

The infrastructure of <u>FORTH</u>'s flux towers and the data from these towers are instrumental in our work. This data is crucial for SUEWS simulations and evaluation processes, enhancing the accuracy and reliability of our analyses. Eddy covariance (EC) is the primary method for directly measuring vertical heat and mass transfers between the Earth's surface and the atmosphere at large scales. It relies on high-frequency data collection of gas concentrations, 3D wind velocities, and is widely used for assessing greenhouse gas fluxes in ecosystems and monitoring responses to climate change and human impacts. FORTH operates two ICOS Associated urban flux towers (https://rslab.gr/fluxtowers.html), one is located in the residential area of Mastambas (HECMAS), while the other is in the Heraklion city center, Kornarou Square, (HECKOR), Crete, established in November 2016 and April 2021, respectively (Figure 1). Both towers are equipped with IRGASONs (Integrated CO_2/H_2O Open-Path Gas Analyzers) and 3D Sonic Anemometers, as well as net radiometers for real-time measurements (online data available: https://rslab.gr/heraklion_eddy.html). In urban areas, EC instruments are located above the typical building height to ensure unobstructed airflow. This allows measurements to represent a substantial portion of the urban surface upwind, known as the flux footprint. Algorithms using wind conditions and surface roughness help identify emission sources and variations in urban covers, such as heating, commuting, and traffic. This aids in defining the footprint's extent (Kljun et al., 2015), (see also CoCO2 del. 3.2, sec. 4.2.1). The initial step involves processing EC datasets with a rigorous quality control procedure to ensure reliable and continuous flux time-series. This includes diagnostic flag assignment to identify and reject low-quality measurements, signal strength assessment to gauge instrument operation, and data filtering while adhering to specified thresholds. Lost F_C measurements are subsequently restored through a gap-filling method, utilizing a moving Look-Up Table (mLUT) approach that considers wind direction, time of day, and day criteria, significantly reducing data gaps.

Additionally, FORTH has built a dense network of meteorological stations throughout Heraklion (https://rslab.gr/wnms.html), from which precipitation data is also collected (https://rslab.gr/heraklion_sensors.html).

The data set utilized for model evaluation in the context of specific urban conditions is sourced from April 2018. All measurements have been aggregated into hourly averages and employed as input for the model. The required data for the present study are:

- Incoming Long-wave radiation (**L↓**: W m^{-2})
- Incoming Short-wave radiation (**K↓**: W m^{-2})
- Air temperature (**T$_{air}$**: $^{\circ}$C)
- Barometric pressure (**p**: kPa)
- relative humidity (**RH**: %)
- wind speed (**U**: m s^{-1})
- precipitation (**P**: mm)

3.2.2 Surface Cover and Flux Footprint Estimation

Footprint modeling is a critical tool for assessing the local geographic area contributing to observed fluxes. The Flux Footprint Parametrization (FFP) model developed by Kljun et al. (2015) is used in this study. It involves two essential input data types: static data, which includes a complete Digital Surface Model (DSM) defining the surface characteristics, such as buildings and trees, and a digital terrain model (DTM) describing the general topography of the surrounding region, which were also used as a surface cover input in SUEWS. The dynamic component of the data is the collected micrometeorology by the EC system. The anisotropic morphology and roughness estimations of 400 m radius around each tower are linked with the 30-min meteorological forcing data from the EC according to the wind direction.

Figure 1 Land cover map of Heraklion. The upwelling source area of EC outline are depicted in black colour 80%.

3.2.3 Traffic and Human Activity Profiles

The calculation of CO$_2$ fluxes involves the careful consideration of both traffic profiles and human activity profiles. The traffic profile is integrated into the SUEWS, which subsequently utilizes it to estimate CO$_2$ emissions. This is particularly critical for HECKOR, where traffic flows play a central role in contributing to CO$_2$ emissions, accounting for approximately 70% of the total emissions on an annual basis. This emphasizes the significance of traffic-related data in understanding and addressing CO$_2$ emissions in urban environments, making it a pivotal aspect of comprehensive emissions modelling and management strategies (Stagakis et al., 2019). To incorporate traffic profiles into the model as outlined in (Leena Järvi et al., 2019), we converted to vehicle kilometers per area per day. Traffic data was obtained through traffic counts using traffic control cables, conducted by the Municipality of Heraklion and TOPOANALYSIS. The study centered on Evans Street, a major road adjacent to HECKOR (Figure 1), effectively capturing city center traffic patterns. The research spanned from July 20 to 29, 2020, and total traffic flow was computed by summing counts from both traffic lanes, subsequently integrated into hourly values for weekdays. To expand the scope of the study

beyond a single street, we incorporated a TomTom monthly product, providing monthly hits at hourly intervals on weekdays for April 2019 representing the number of measurements in the vicinity of HECKOR, as indicated by colorized roads in Figure 1. We then made the assumption that Heraklion's traffic flows remain consistent throughout the year. Consequently, we established a correlation between two sets of traffic flows from the same road, depicted in Figure 1, based on traffic control cables. The correlation demonstrated a strong linear fit with an R-squared value of 0.89.
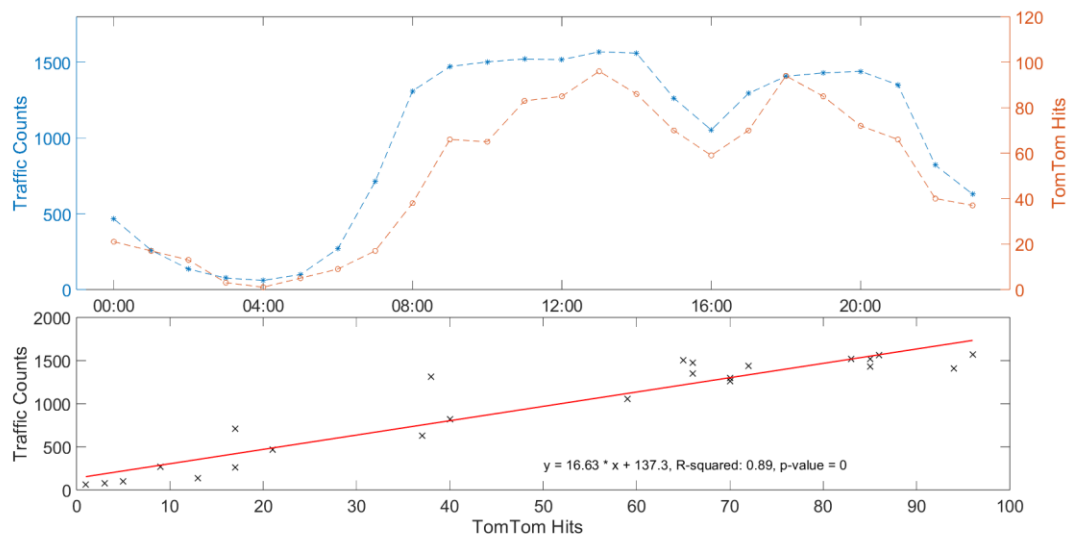
Figure 2 Traffic daily patterns for weekdays (Traffic control cables: blue, TomTom Hits: orange). At the bottom, a strong linear fit with an R-squared value of 0.89

Subsequently, each road extracted from the TomTom product was buffered to a width of 1 meter. The data was then rasterized so that each grid cell contained hits converted to units of vehicles per square meter per hour. The next step involved assigning weights to each grid cell based on their frequency of occurrence, with those cells having higher frequency contributing more significantly to CO_2 emissions, reflecting a higher likelihood of emissions being measured. Lastly, we applied the equation obtained from the linear regression between the two traffic profiles, as it was evident that while the TomTom traffic hits did capture daily patterns, they did not align qualitatively with the measured traffic counts.

Regarding the human activity profiles, it is assumed that the residential population density determines the nighttime activity and that the daytime activity is double the amount of the nighttime activity (Leena Järvi et al., 2019).
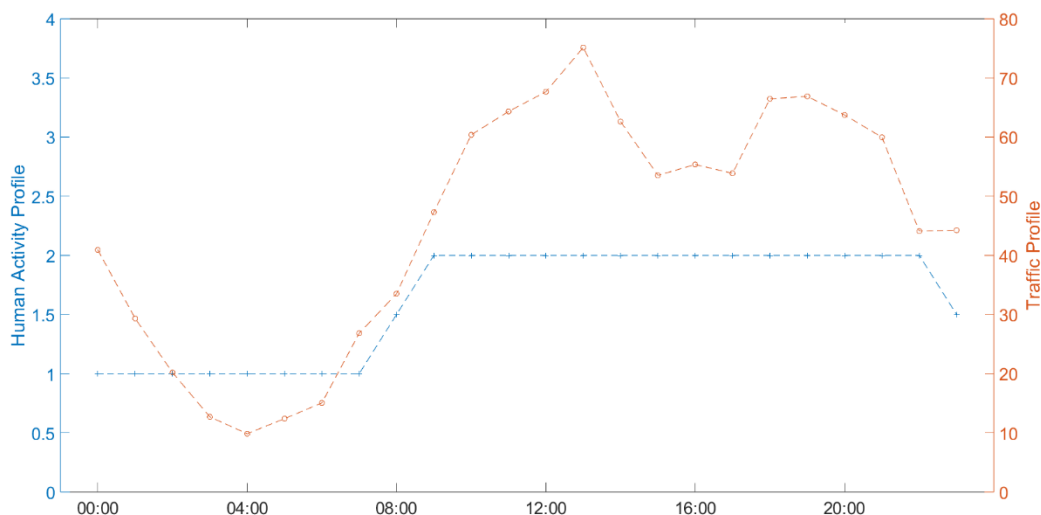
Figure 3 Traffic and Human Activity Profile used as inputs in SUEWS.

3.3   Model evaluation

The SUEWS model (v. 2020b) is employed to simulate a range of fluxes within the city of Heraklion. The model is meticulously evaluated against actual data obtained from the EC tower, with a specific focus on assessing local and neighborhood-scale fluxes and designed to align with the FFP. The simulation corresponds to version 3.15.4 UMEP and operates offline with a 5-minute time-step. To meet the model's data requirements, all beforementioned inputs are set at a resolution of 60 minutes, with linear interpolation applied at 5-minute intervals for most parameters. Model outputs are averaged to 60 minutes to ensure comparability with the F_c.

The ultimate outcome of the SUEWS model yields five distinct output variables:

- **F_c** : Total CO_2 fluxes [umol m^{-2} s^{-1}]
- **F_c Build**: CO_2 fluxes from buildings [umol m^{-2} s^{-1}]
- **F_c Metab**: CO_2 fluxes from metabolism [umol m^{-2} s^{-1}]
- **F_c Photo**: CO_2 fluxes from Photosynthesis [umol m^{-2} s^{-1}]
- **F_c Traff**: CO_2 fluxes from traffic [umol m^{-2} s^{-1}]
- **F_c Respi**: CO_2 fluxes from respiration [umol m^{-2} s^{-1}]

In the concluding step, a linear regression is employed to establish a correlation between the F_c obtained from HECKOR and the F_c derived from SUEWS. This analysis reveals a robust linear fit with an R-squared value of 0.81, indicating a significant association between the two sets of data.

In summary, the traffic profiles obtained effectively explained the expected daily F_c pattern with high reliability, except for the morning peak. For HECKOR, the daily F_c pattern was previously described in (Stagakis et al., 2019), with the highest peak occurring around midday, followed by a temporary decrease in the afternoon and a second distinct peak in the early evening following the business-commercial and working hours.

In contrast, the SUEWS model exhibits a distinct pattern with two peaks of similar magnitude occurring around midday and evening, followed by a decrease in the afternoon and nighttime. When examining all the output variables of SUEWS, a strong correlation is observed between the total F_c and F_c Traffic, which aligns with expectations based on previous studies (Stagakis et al., 2019) suggesting that traffic plays a substantial role in the total annual F_c, contributing

to approximately 70% of the total. However, it is worth noting that the peaks in F_c Traffic do not correspond to the height of the measured F_c at HECKOR.
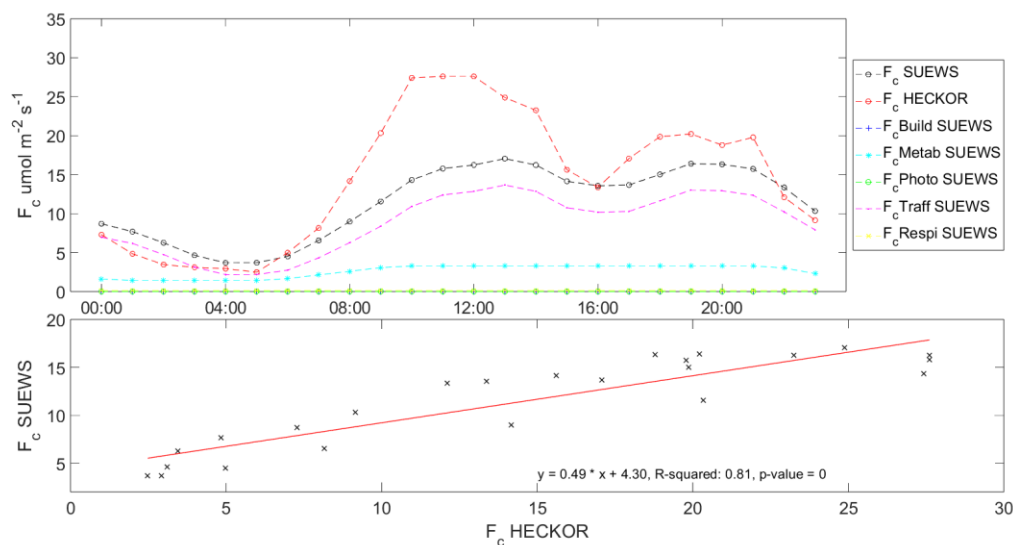
Figure 4 F_c Weekday profiles (top) and a strong linear fit with an R-squared value of 0.81

One possible explanation is that there may be variations among the vehicles passing nearby, such as differences in the type of fuel they use and the vehicle types. For instance, during the early peaks, there may be more trucks transporting products to local markets or business districts, and buses assisting with commuter transportation which emits more CO_2 than regular cars. Regarding F_c Photo, as previously mentioned in (Chrysoulakis et al., 2023),the sparse vegetated areas can lead to the observation of negligible fluxes. F_c Metab appears to follow human activity patterns, suggesting that a similar number of people visit the city center in the morning for business or commercial purposes and in the evening for leisure activities, such as walking or enjoying a coffee. As for F_c Building, during April, the high temperatures in Heraklion may account for the negligible values as there is no emissions used for i.e. heating purposes.

This continuous and comprehensive monitoring system provides valuable insights into sectorial fluxes, allowing for a detailed understanding of the diverse sources and dynamics of CO_2 within the urban landscape. In the subsequent stages, it would be advantageous to enhance the monitoring of the SUEWS model by incorporating additional inputs, such as detailed information about the types of vehicles that are present in Heraklion, including their temporal distribution throughout the entire year. One of the notable strengths of this flux tower system lies in its adaptability to multiple sites and its capacity for evaluation alongside other flux towers. This adaptability ensures that the system can be employed in various urban settings, contributing to the collective knowledge of urban microclimates and emissions.

Further model development can yield well-evaluated values in 100m grids around HECKOR, consequently enhanced understanding of sources and sinks supports correlations with other atmospheric models like (McNorton et al., 2023), as well as the unique diFUME approach. The sustained data continuity of HECKOR, with a rigorously validated model establishes a solid groundwork for the execution of correlation of CO_2 inversion studies and/with alternative atmospheric models facilitating comprehensive investigations into urban microclimates and CO_2 emissions.

4 diFUME model

4.1 Model description

diFUME is a recently developed urban CO_2 flux model designed for high spatiotemporal resolution simulations of the local CO_2 balance within urban areas (Stagakis, Feigenwinter, Vogt, & Kalberer, 2023). The model is designed for applications which aim to interpret, link or compare local urban CO_2 concentration or CO_2 flux measurements with modelled estimations. The model is divided in four main modules which simulate hourly:

1. Building emissions
   a. emissions related to space heating (E_B)
   b. emissions from commercial/industrial buildings not related to space heating (E_C)
2. Vehicle traffic emissions (E_V)
3. Human respiration emissions (R_H)
4. Biogenic CO_2 exchange ($F_{C,B} = R_S + R_V - P_V$, where R_S: soil respiration, R_V: plant respiration and P_V: photosynthetic CO_2 uptake).

The local CO_2 flux (F_C) is computed by summing all terms, similarly as Eq. 3.

Even though the model takes into account industrial building emissions, it is not explicitly designed to model the emissions from industrial areas which are often located outside the main city boundaries. Industry sector-specific emissions and large chimney emissions are not included in the model simulations. Moreover, agriculture, farming and waste management emissions that can be significant in the outskirts of the cities are not considered in this model.

The diFUME model is based on open geospatial datasets, census information, road traffic data and basic meteorological parameters. The main geospatial inputs for the Basel case study are:

i)   a detailed land cover map which discriminates building categories (i.e. residential, workplaces, mixed, commercial/industrial), road types (i.e. main roads, collecting roads, settlement roads, restricted traffic areas), paved surfaces and green areas,
ii)   high resolution Digital Surface Models (DSMs) for buildings and trees
iii) daytime and night-time population density maps, and
iv)   Leaf Area Index (LAI) time-series based on Copernicus Sentinel-2 (S2) imagery.

4.2 Model inputs and calibration

The diFUME model is parametrised for the city center of Basel based on several input datasets. A full description of the parametrisation is provided in (Stagakis, Feigenwinter, Vogt, & Kalberer, 2023). Here, a brief description of the main input parameters is given.

4.2.1 Land cover and Digital Surface Models (DSMs)

A land cover map (including land-use types) of the study area at 1 m resolution is produced combining multiple sources of information. The main source is the official survey map of Basel-Stadt of 2019 (Amtliche Vermessung Basel-Stadt, 2021), which serves as the base map for all additional information. The information of tree crowns is then treated as an additional level of overlying information based on the data of the airborne LiDAR campaign of 2018. The buildings are further categorized as pure residential, partly residential (i.e. mix of residential and workplace), workplaces and commercial/industrial according to Basel-Stadt map of building types (Gebäudeadressen und -informationen, 2022) and the Urban Atlas (GMES/Copernicus land monitoring services, 2018). The commercial/industrial class is assigned to the buildings that are located inside the respective Urban Atlas polygons, classified by the Basel-Stadt building type map as partly residential (defined as 50 % commercial/industrial) and workplace (defined as 100 % commercial/industrial). The road type

classification of the city authorities (Strassen Wege, 2022) and the vehicle traffic zones (Verkehrsberuhigte Zonen, 2022) are used to derive a street classification scheme that is meaningful for vehicle emission modelling. Traffic-oriented roads inside the study area are classified as main roads and collecting roads. Settlement-oriented roads are usually under special restrictions and therefore are classified as settlement roads (no special restriction), Tempo 30 (30 km/h limit) and meeting zones (20 km/h limit). The rest of the roads are restricted to motor vehicles and classified as pedestrian roads.

The urban morphology of the study area is characterized combining three surface-object models. The Digital Terrain Model (DTM) describes the elevation (m above sea level) of the ground, ignoring any object (e.g. buildings or trees) and is used with a 1 m resolution (Terrainmodell - DTM, 2022). The building heights (m above ground) are produced using the 3D model of the city, provided in vector format (3D-Stadtmodell, 2021). The tree heights (m above ground) are estimated using an aerial LiDAR dataset acquired in summer 2018. Digital Surface Models (DSMs) for buildings, trees and their combination are produced by adding the respective height products on the DTM. When adding both elements on the DTM to represent the full DSM, the higher element is kept for the pixels where buildings and trees overlap.

4.2.2 Leaf Area Index (LAI)

Copernicus Sentinel-2 (S2) imagery is used for the monitoring of urban vegetation LAI. S2 mission provides revisit time of 5 days using a constellation of two identical satellites S2A and S2B. The Level 2A (L2A) product by the Theia Land Data Centre of CNES (Centre national d'études spatiales) is used, which provides georeferenced and orthorectified surface reflectance (SR), water vapor content (WVC), aerosol optical thickness (AOT), cloud and geophysical masks, processed by the MAJA atmospheric processing software (Hagolle et al., 2017). The 10 m SR bands in red (SR_{red} : 665 nm) and near-infrared (SR_{NIR} : 842 nm) are used to compute NDVI (Normalized Difference Vegetation Index) as $(SR_{NIR} - SR_{red})/(SR_{NIR} + SR_{red})$ and the product is masked for clouds, cloud shadows and snow according to the L2A product flags. NDVI is converted to LAI values by applying an empirical exponential formula (Stagakis et al., 2015) and is then resampled from 10 m to 5 m resolution, enhancing the initial LAI values, using the vegetation fraction derived by the 1 m Land Cover products at 10 m ($\lambda_{v,10m}$) and 5 m ($\lambda_{v,5m}$) grids as:

$$LAI_{5m} = LAI_{10m} \cdot \frac{\lambda_{v,5m}}{\lambda_{v,10m}} \qquad \qquad (4)$$

For Eq. 4 to be applicable, $\lambda_{v,10m}$ and LAI_{10m} are first resampled to 5 m without changing their initial values (i.e. 2 x 2 neighbouring pixels of the same value). Equation 4 works when $\lambda_{v,10m}$ is not zero, thus in areas where vegetation fraction is zero, LAI_{5m} is also set to zero. The produced LAI imagery (5-day interval at optimum conditions) is then temporally linearly interpolated on a pixel by pixel basis to produce daily gap-filled imagery. In order to reduce the random noise on the timeseries, a moving 15-day maximum value composite filter is applied per pixel to the daily LAI timeseries.

4.2.3 Meteorological data

Table 1 summarizes the station locations and the respective input meteorological variables that are used in this application, as well as the instrumentation used for each measurement. Air temperature (°C) and vapor pressure (kPa) are measured on a micrometeorological tower located near the centre of the study area and are considered uniform across the site. Vapor Pressure Deficit (VPD, kPa) is then calculated based on saturated vapor pressure estimation (Buck, 1981). Direct and diffuse incoming radiation are measured with a 2-axis sun tracker (INTRA, BRUSAG) at the roof-level in an unobscured location next to the micrometeorological tower. Measured shortwave radiant flux densities (W m^{-2}) are converted to photon flux

densities (µmol m^{-2} s^{-1}) within PAR (i.e. photosynthetic active radiation, solar shortwave radiation between 400 – 700 nm) using the conversion factor suggested by MacKerron (2005). Soil temperature (°C) and volumetric water content (m^3 m^{-3}) are continuously measured at three different locations of the study area at 10 cm below surface. The locations have different characteristics, BKLI is at a street canyon, BKFP is at a non-irrigated park location and BSMP is at an irrigated park location.

Table 1. Meteorological stations and variables that are used as inputs to the models.

Station acronym	Geographic location	Variables	Sensor type - model	Sensor height (m a.g.l.)
BKLI	47.56173 °N, 7.58049 °E	Air temperature Vapor pressure Direct radiation Diffuse radiation Soil temperature-moisture	Thermo-HYGrometer (Thygan) Thermo-HYGrometer (Thygan) Pyrheliometer (CHP1, Kipp & Zonen) Pyranometer (CM21, Kipp & Zonen) Thermistor - Water content reflectometer (CS655, Campbell Scientific Inc.)	38 38 21 21 -0.1
BKFP	47.56595 °N, 7.56921 °E	Soil temperature-moisture	Thermistor - Water content reflectometer (CS655, Campbell Scientific Inc.)	-0.1
BSMP	47.5529 °N, 7.57456 °E	Soil temperature-moisture	Thermistor - Water content reflectometer (CS655, Campbell Scientific Inc.)	-0.1

4.2.4 Vehicle traffic

Traffic counts per hour and vehicle type are available online for 31 permanent locations across the city (Verkehrszähldaten motorisierter Individualverkehr, 2022). The available data from the permanent locations and short-term surveys in Basel-Stadt since 2010 (Verkehrszähldaten, 2022) were used to extract annual diurnal profiles (weekend and weekday) from all the available surveys according to road types. This analysis is used to estimate the hourly traffic of each vehicle type. Main and collecting roads are separated in several segments according to the main road junctions. The other road types are considered uniform (i.e. each road type represents one segment). Road segments equipped with a traffic station are attributed with the hourly measured vehicle count data, while the rest are attributed with the mean hourly count of all stations of the specific road type, assuming homogeneous spatial profiles for each road class.

4.2.5 Population density

Annual statistics per city block on residential population (by age group) and workplace employees (Beschäftigte und Arbeitsstätten, 2021; Wohnbevölkerung, 2021) are used to derive maps of annual night-time and daytime building-scale population density (inhabitants per m^2 or inh. m^{-2}) for weekdays and weekends. Considering the building type (i.e. residential, partly residential, workplace), building volume is separated to residential volume and workplace volume, so that population is redistributed between night-time, daytime, workdays and weekends.
Night-time building population density is considered the same for weekdays and weekends and is estimated per building by scaling the total block resident population according to building volume. Weekday and weekend daytime building population density is estimated by involving the distribution of block population by age, to calculate the inhabitants that stay home

during day, and the number of employees per block to calculate the population that occupy the working places.

4.2.6 Building emission model calibration

Average monthly HDH and monthly energy consumption for district heating in Basel are presented in Fig. 5. This dataset is used as a proxy to estimate the total monthly consumption for building heating by the residential sector (Fig. 5b). A single conversion coefficient is established for each reference year, applied to the monthly values of each respective time period.
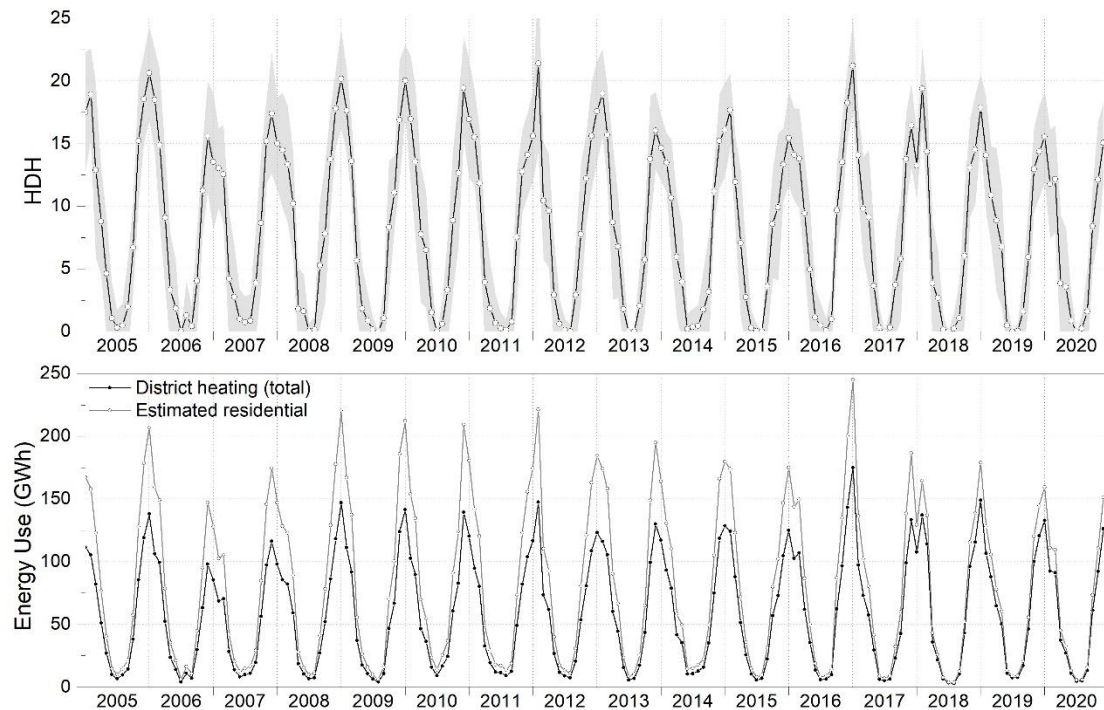
Figure 5 Time-series of (a) monthly mean and standard deviation of Heating Degree Hours (HDH) for the area of Basel, (b) monthly energy consumption for district heating (residential + commercial/industrial) and estimated total energy consumption for heating by the residential sector of Basel-Stadt.

The monthly estimated energy consumption for residential heating (in GWh) is converted to mean hourly consumption (in Wh) and then divided by the total occupied building volume for residential use in the city of Basel-Stadt area for each respective year to express the consumption per building volume (Wh m^{-3}). The regression between the estimated mean hourly consumption per building volume and monthly average HDH for the period 2005 – 2020 (Fig. 6) reveals that the heating consumption by residential buildings is nearly linearly dependent on the HDH.
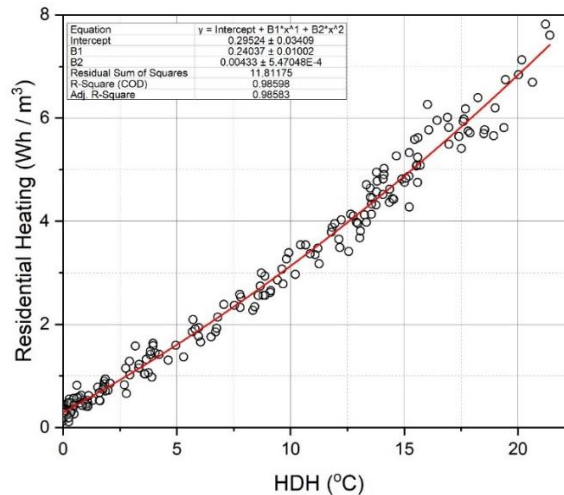
Figure 6 Regression between Heating Degree Hours (HDH) and building energy consumption for heating of the residential sector expressed per m³ of building volume.

4.3   Model evaluation

4.3.1   Study area and eddy covariance stations

The area of the diFUME model application is the city centre of Basel, Switzerland, defined by a rectangle of 3 km x 3 km which includes two eddy covariance (EC) stations (Fig. 7). The first EC station (BKLI) is located on an 18 m tower, installed on the roof of a 20 m university building and has been operational since 2004. The system is mounted on a vertical extension at the top of the tower, reaching a total receptor height of 39 m above street level. The second EC system (BAES) is located on the top of a building over a busy central square, operated since 2009. The system is installed on a flagpole on top of a small construction over the building's rooftop at 41 m above street level. System specifications are described in Table 2 and more details on system set-ups, relations to local surroundings, maintenance, calibration and raw data logging can be found in Schmutz et al. (2016), Lietzke et al. (2015) and Lietzke and Vogt (2013).

Table 2 Eddy covariance system information used for the evaluation of diFUME model in Basel.

Station acronym	Geographic location	Sensor height (m a.g.l.)	Sensor models (sonic anemometer, gas analyser)	Sonic azimuth (°)	Acquisition frequency (Hz)
BKLI	47.56173 °N, 7.58049 °E	39	HS-100 (Gill Instruments Ltd.), LI-7500 (LI-COR Inc.)	0	20
BAES	47.55123 °N, 7.59560 °E	41	CSAT3 (Campbell Scientific Inc.), LI-7500 (LI-COR Inc.)	340	20

4.3.2   Eddy covariance data processing

Raw EC data of both systems are processed at 30-min time-steps for the study period (2018 – 2020) using the EddyPro® Software v7.0.6 (LI-COR Inc.). The main processing steps include axis rotation for tilt correction using the double rotation method (Kaimal & Finnigan, 1994), linear detrending to extract turbulent fluctuations (Gash & Culf, 1996), covariance maximization for time-lag compensation between the gas analyser and the sonic anemometer

(Fan et al., 1990) and density fluctuation compensation according to Webb et al. (1980). Spectral corrections are also applied to flux estimates for low and high frequency losses. Analytic correction of high-pass filtering effects is applied according to (J. Moncrieff et al., 2004) and correction of low-pass filtering effects is applied according to Moncrieff et al. (1997). Furthermore, statistical analyses are performed on the raw data to filter out spikes (Vickers & Mahrt, 1997), drop-outs and extreme values. Quality flagging is performed according to steady state and integral turbulence characteristics tests (Foken et al., 2004; Foken and Wichura, 1996; Göckede et al., 2008) based on the 3-point flagging system of (Mauder, M. & Foken, 2004). Time-periods with the quality flag of 2, around rain events (1 hour before and 3 hours after precipitation recordings) and during maintenance activities are rejected. Additionally, gas analyser warning flags are used as indicators of problematic measurements. If more than 10 % of the raw data are missing or flagged by any warning flag, then the values are rejected. F_C measurements under low turbulence situations are also removed from further analysis by setting a lower threshold to friction velocity $u^* = 0.15$ m s^{-1} (e.g. Järvi et al., 2012; Matese et al., 2009; Salgueiro et al., 2020). The data availability during the three-year period 2018 – 2020 after the filtering reaches 64 %, where 3 % of data loss is due to maintenance and technical failures, 15.5 % is due to rain events and 17.5 % is due to the quality flags and the other filters.
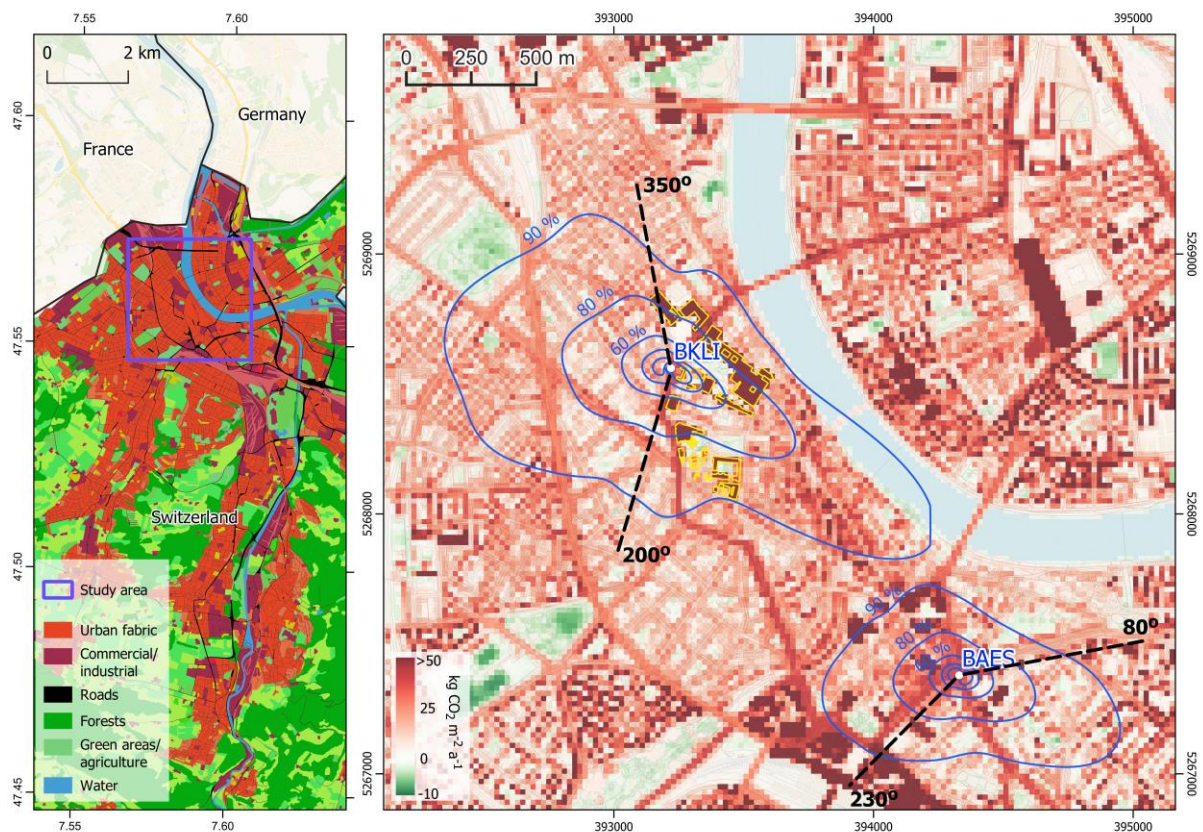
Figure 7 The location of the study area (left) over an Urban Atlas land cover type representation. Eddy covariance site locations (right), along with the long-term source area isopleths, over the diFUME modelled annual CO₂ flux map for 2018 at 20 m resolution. The main wind direction sectors attributed to different land use profiles are indicated. University and hospital buildings are indicated with yellow polygons. All maps are projected at UTM 32N (EPSG: 32632).

4.3.3 Source area modelling

The FFP is used for the estimation of flux source areas for the two tower sites. DSMs for buildings and trees, as well as the DTM in 1 m resolution are used as input for the Urban Multi-scale Environmental Predictor (UMEP) Morphometric Calculator tool (Lindberg et al., 2018) to estimate roughness length (z_o) and the zero-plane displacement height (z_d) around each EC

site. The morphological inhomogeneity of the urban surroundings is considered in the source area modelling by adopting a directional roughness parameterisation scheme. z_o and z_d are estimated anisotropically for all wind directions (averaged to 5° wind sectors) to a radius of 400 m around each EC tower according to the real urban surfaces parameterization of Kanda et al. (2013). Roughness parameter Look-Up-Tables (LUTs) are then developed for defining z_o, z_d inputs to FFP according to wind direction. z_d is an indirect input for the model, since the measurement height is defined in FFP as $z_m = z_{receptor} - z_d$. The other FFP inputs are i) wind direction, ii) standard deviation of lateral velocity fluctuations, iii) friction velocity (u*), iv) Obukhov length (L) and v) planetary boundary layer height (PBLH). Wind attributes, u* and L are calculated during the EC data processing. The Monin-Obukhov stability parameter (z_m/L) is used for the indication of atmospheric stability regime. PBLH is estimated for each 30 min period using diagnostic formulas to provide the initial height during night-time stable and neutral conditions (Nieuwstadt, 1981; Zilitinkevich et al., 2012) and then a simplified turbulence kinetic energy equation for convective conditions to determine the rate of change of PBLH for each 30-min period during convective daytime conditions (Batchvarova & Gryning, 1991).

FFP runs for each site at 1-hour time-step, considering two consecutive EC measurements as inputs on every run, at spatial domains of 2 x 2 km centred at each tower location and at 20 m spatial resolution. The gridded footprint function values $f_{(x,y)}$ are normalized according to the domain sum to be used as spatial weighting grids ($\varphi_{(x,y)}$):

$$\varphi_{(x,y)} = \frac{f_{(x,y)}}{\sum_{x,y=1}^{x,y=N} f_{(x,y)}} \tag{5}$$

Where, (x, y) represent the grid cells of the footprint and N represents the total number of grid cells at vertical and horizontal directions for the entire domain area of each footprint (2 km x 2 km).

4.3.4 Comparison between observations and model

The comparison between the EC-derived $F_{C,obs}$ and the hourly modelled gridded fluxes (E_B, E_C, E_V, R_H, $F_{C,B}$) is achieved by spatially aggregating the gridded maps according to the normalised footprint functions:

$$F_{C,model} = \sum_{x,y=1}^{x,y=N} \varphi_{l(x,y)} \left[f_B \cdot E_{B(x,y)} + f_C \cdot E_{C(x,y)} + E_{V(x,y)} + R_{H(x,y)} + F_{C,B(x,y)} \right] \tag{6}$$

Where, $F_{C,model}$ is a source area aggregated CO$_2$ flux model estimate; (x, y) represent the grid cells of the footprint and flux products; N represents the total number of grid cells at vertical and horizontal resolution for the entire domain area of each footprint (2 km x 2 km); $\varphi_{(x,y)}$ is the footprint weighting grid of the same resolution as the BU model outputs; $E_{B(x,y)}$, $E_{C(x,y)}$, $E_{V(x,y)}$, $R_{H(x,y)}$, $F_{C,B(x,y)}$ are gridded diFUME model outputs; and f_B, f_C are normalization factors of the building emission maps. The f_B and f_C normalisation factors are used to account for the spatial variability of building emissions within the flux footprints. BU emissions models represent building emissions as spatially homogeneous across the building extents (Stagakis, Feigenwinter, Vogt, & Kalberer, 2023), whereas in reality the building emissions occur at specific points in space according to the location of the building or neighbourhood energy units and the respective chimneys. This inconsistency leads to overestimation of footprint-weighted E_B and E_C because building area is always present in flux footprints but actual building emissions are not necessarily within the footprint at all times. The following empirical formula is used:

$$f_i = \frac{\sum_{x,y=1}^{x,y=N} \lambda_{i(x,y)} \cdot M_{90(x,y)}}{MAX_i} \tag{7}$$

Where, $\lambda_{i(x,y)}$ represents the fraction of buildings according to the land cover map ($i: B$ for non-commercial/industrial buildings, $i: C$ for commercial/industrial buildings) at (x, y) grid cell; $M_{90(x,y)}$ is a spatial mask of Boolean values (0,1) which defines the 90 % cumulative footprint area; and MAX_i is an empirical maximum value of accumulated building fractions which depends on the spatial resolution of the grid (x, y). At 20-m resolution, MAX_B is set to 400 and MAX_C is set to 150. Eq. 7 follows the reasoning that when the atmospheric conditions favour spatially extended footprints towards building-occupied areas, then the probability of $F_{C,obs}$ to be affected by building emissions is higher than when the footprint is small and restricted near the tower location or directed towards open areas.

Hourly statistics are derived for two different wind sectors and each EC site. Azimuth angles 350° and 200° define the wind sectors BKLI-E (east) and BKLI-W (west), while the angles 80° and 230° define the wind sectors BAES-E (east) and BAES-W (west) (Fig. 7). Data are also clustered according to seasons (roughly indicated as winter and summer) and type of day (weekdays, weekends). Summer period is considered as May to September and winter period includes the rest of the months.

4.4   Results

4.4.1 Model outputs

Fig. 8 presents the time-series of daily fluxes for the whole study area. There is intense seasonal variability in the total CO_2 flux (F_C) captured by the model. The study area behaves as a CO_2 source during all seasons (Fig. 8a), while F_C is approximately doubled during winter following the acute rise of building emissions (E_B) due to space heating (Fig. 8b). E_B daily variability during winter is driven by the respective temperature changes. The contrast between weekdays and weekends is obvious in the F_C (Fig. 8a), which is caused by E_V, E_C and partly R_H variability (Fig. 8). Traffic is a less important source than buildings in our study area, especially during winter. Even though it is not very obvious in the spatial averages, E_V can be a very important CO_2 source along the main roads. E_V presents repetitive weekly and seasonal patterns, with low emissions during weekends and the Christmas holidays.

The effect of the COVID19 lockdown during March-May 2020 is clearly visible in Fig. 8b, where the lowest E_V over the entire three-year period is detected. After May 2020, E_V increases again, but does not reach the levels of the previous years. R_H is relatively steady during the whole year, increasing during weekdays due to the incoming working population. Biogenic flux ($F_{C,B}$) presents clear seasonal patterns following meteorology and plant phenology. Winter is a dormant period for all biogenic components and green areas behave as weak CO_2 sources. Photosynthesis rises during Spring and peaks during early Summer. During this period, green areas are behaving as carbon sinks. During late summer there is a decreasing tendency for plant productivity mainly due to drought conditions, which can be variable between different years (Fig. 8c).
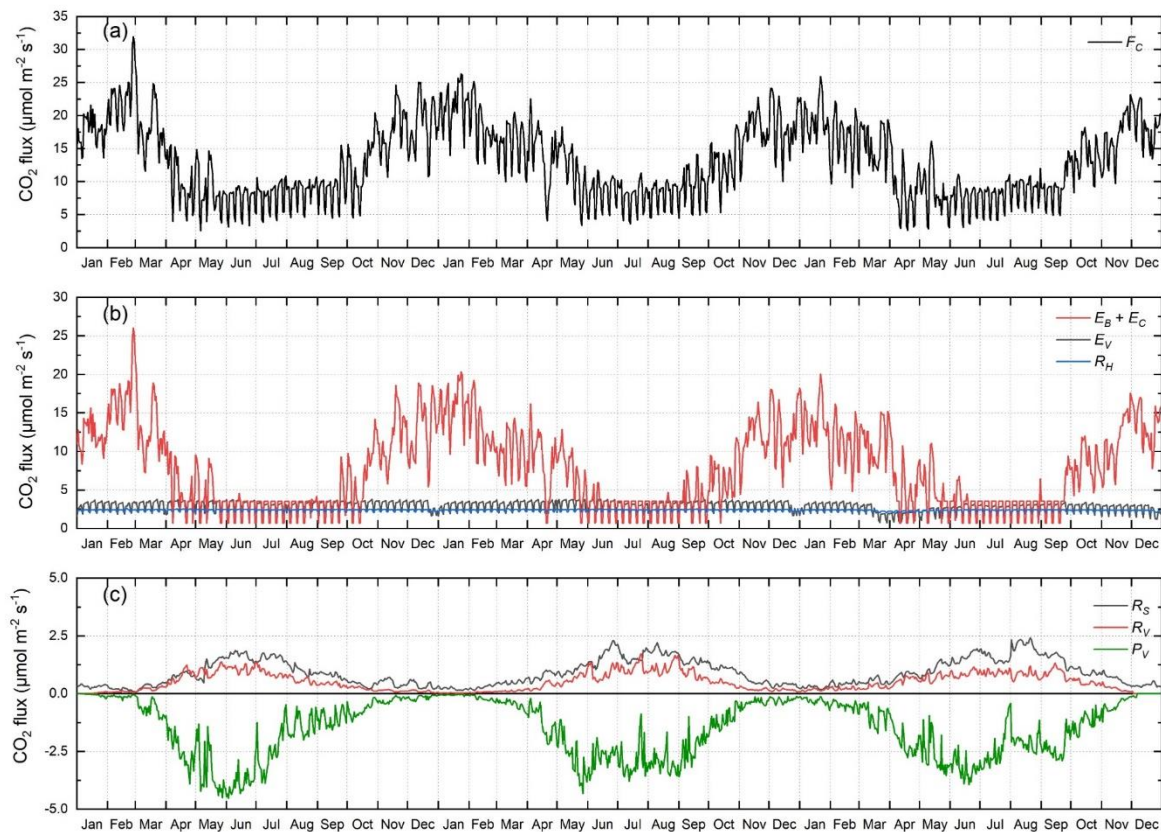
Figure 8 Time-series of the daily modelled mean CO_2 flux of the study area (μmol CO_2 m⁻² s⁻¹) for the period 2018 – 2020. (a) Total CO_2 flux (F_C), (b) building emissions (E_B, E_C), traffic (E_V), human respiration (R_H) and (c) the biogenic flux components (R_S, R_V, P_V). Note that the y-axis scaling is different for each plot and specifically for the biogenic fluxes.

The diurnal variability of the modelled components is summarized in Fig. 9 for winter and summer months, separated to weekdays and weekends. There is a clear diurnal pattern at weekdays during the whole year with lower emissions during night, a sudden rise early in the morning and then gradually decreasing emissions over the day (Fig. 9a,c). This pattern is driven by the mixture of the different F_C components. E_V shows an early morning and an evening peak throughout the year (Fig. 9a,c). E_B during winter (Fig 10a) shows highest emissions during night and early morning and lower during day, while its contribution during summer is minimal (Fig. 9c). Biogenic CO_2 fluxes contribute only slightly to the winter diurnal pattern (Fig 9a), but during summer (Fig. 9c) they strongly affect the diurnal pattern by reducing F_C during day and increasing it during night.

The diurnal F_C patterns during weekends (Fig. 9b,d) present different cycles compared to weekdays, with higher emissions during night and lower during day. This is especially pronounced during summer due to the reduced E_B and the increased photosynthesis (Fig. 9d). Weekend E_V does not present the morning rush hour peak that is obvious during weekdays and therefore its maximum is later during the day compared to weekdays. During winter, weekend F_C remains high during the whole 24h, while a slight decrease during day is mainly due to E_B (Fig. 9b).

D7.10 New measurement and modelling methodologies for high resolution monitoring of urban anthropogenic and biogenic CO_2 fluxes
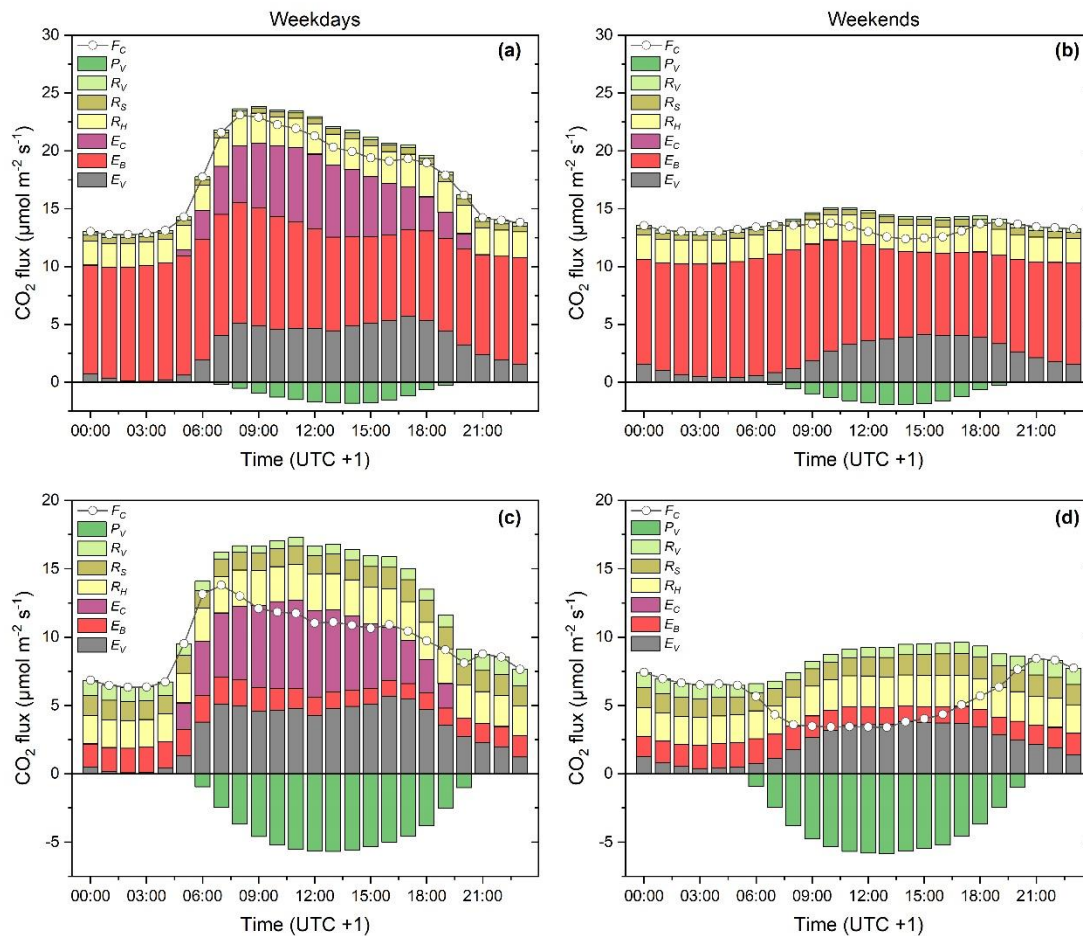
Figure 9 Diurnal hourly mean profiles of each modelled CO₂ flux component and the total F_C for the study area for the periods: (a) winter weekdays, (b) winter weekends, (c) summer weekdays, (d) summer weekends. Building: E_B, commercial/Industrial: E_C, traffic: E_V, human respiration: R_H, soil respiration: R_S, plant respiration: R_V, plant photosynthesis: P_V.

The annual total CO₂ emissions per model component for the study area and the year 2018 are listed in Table 3. Buildings have the greatest share of emissions, contributing 60 % to the total CO₂ balance. Even though traffic emissions can be very high in some road segments, the total contribution to the total study area (23.5 %) is much lower than the building emissions, while human respiration contributes significantly to the total budget (18 %). Photosynthesis has also a significant share in reducing the emitted CO₂ (10.4 %), but when considering plant/soil respiration in the annual scale, the biogenic balance reduces the anthropogenic emissions only by 1.6 %.

Table 3 Annual flux totals for 2018 (kg CO$_2$ m^{-2} a^{-1}) and percent contribution per modelled flux component for the study area.

Building heating emissions	E_B	8.2	44.8 %	}	Buildings	11.0	60.1 %
Commercia/Industrial emissions	E_C	2.8	15.3 %				
Vehicle emissions	E_V	4.3	23.5 %	=>	Traffic	4.3	23.5 %
Human respiration	R_H	3.3	18.0 %	=>	Human	3.3	18.0 %
Soil respiration	R_S	1.0	5.5 %	}			
Plant respiration	R_V	0.6	3.3 %		Plants/Soil	-0.3	-1.6 %
Plant photosynthesis	P_V	-1.9	-10.4 %				
Total	F_C	18.3	100%			18.3	100%

4.4.2 Model evaluation

The model is evaluated using the observations of the two EC sites at the different wind sectors. This analysis provides an overview of the model performance for different periods and emission typologies. Fig. 10 gives an overview of the diurnal profiles of the different wind sectors concerning observed ($F_{C,obs}$) and modelled ($F_{C,model}$) fluxes. Each wind sector has unique source/sink characteristics. There is a good agreement between the model and the observations in all wind sectors but modelled estimates provide either overestimations or underestimations depending on the source/sink characteristics of each wind sector. In general, we can see that the high emissions cases tend to be underestimated and the low emission cases, overestimated. For example, BKLI-E presents high emissions as a mixture between traffic and building emissions, and the modelled values do not follow these high emissions during day. On the other hand, BKLI-W is a residential area with not a lot of main roads, so the emissions are low during the whole year. The modelled values tend to overestimate the emissions from this area, especially during night. Exceptionally good agreement is demonstrated in the BAES-W (Fig. 10m,o), where E_V is the dominant emission source. Inconsistencies between $F_{C,obs}$ and $F_{C,model}$ are big in some cases, such as during summer weekends in BKLI-E (Fig. 10d) and BAES-E (Fig. 10l). In BKLI-E there is an obvious underestimation during morning hours, which is caused by the early onset of photosynthesis and the late rise of E_V (Fig. 10d). On the contrary, in BAES-E there is an obvious overestimation of daytime F_C (Fig. 10l), which could be due to photosynthesis underestimation in this sector.

The statistical metrics and comparison plots between $F_{C,obs}$ and modelled F_C $F_{C,model}$ for different seasons, day types, sites and wind sectors are presented in Table 4. The mean differences range from -3.8 to 3.6 µmol CO$_2$ m^{-2} s^{-1}. In most cases, the deviations between the means are proportionally higher during weekends. The hourly metrics, aggregated between seasons and day types, show mean absolute errors (MAE) ranging from 5.0 to 7.1 µmol CO$_2$ m^{-2} s^{-1} and root-mean-square errors (RMSE) ranging from 7.4 to 10.2 µmol CO$_2$ m^{-2} s^{-1}. These results are very promising and indicate that the model is able to capture very well both the spatial and temporal variability of the urban CO$_2$ fluxes.

It is demonstrated that the BAES-W, which is an area dominated by traffic emissions, is also the area that the model agrees very well with the observations. In contrast, the model does not perform so well in the rest of the areas where we have a mixture of building, traffic and biogenic flux processes. These outcomes indicate that traffic spatiotemporal emission patterns are in general more effectively captured by the model, while the rest of the components are more difficult to model, especially building emissions and biogenic CO$_2$ fluxes. Even though the vehicle emission model does not take into account spatially resolved estimations of driving mode, vehicle speed, congestion, idling or environmental effects, the emissions estimates are fairly realistic.
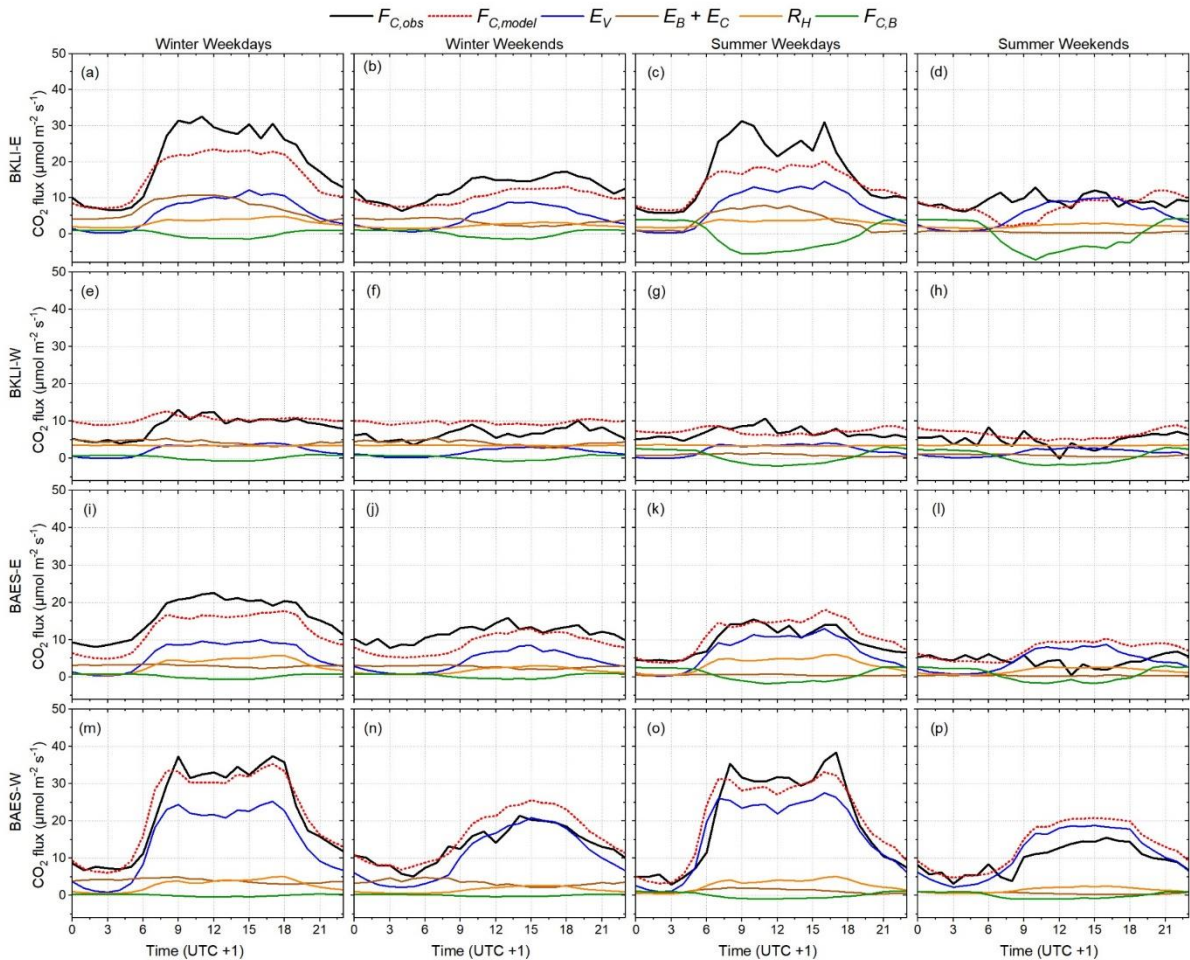
Figure 10. Diurnal hourly mean profiles of eddy covariance measured F_C ($F_{C,obs}$) and source area aggregated modelled F_C ($F_{C,model}$) estimations, as well as five modelled components (E_B+E_C, E_V, R_H, $F_{C,B}$). The profiles are presented separately for winter weekdays (1st column), winter weekends (2nd column), summer weekdays (3rd column) and summer weekends (4th column) for the two wind sectors (W,E) of each eddy covariance site (BKLI, BAES).

Emissions from a city can be much more complex than represented in the model. Because the model is designed for city-scale applicability and focussed on the local surface CO_2 fluxes, it presents several restrictions. The building emission part of the model relies on general temporal and spatial proxies (i.e. single heating energy consumption function, building volume/type) and therefore cannot describe the variability induced by the various building typologies and energy use efficiencies. The characterisation of the emissions by commercial/industrial activities is further simplified and does not consider the types of activities which would define the emission rates. Therefore, the model outputs are not ideal for extracting building-level planning decisions, such as energy renovation strategies. It is therefore expected that the model can provide a general spatiotemporal overview of the emissions per road type but not explicitly locate and characterise driving condition and road network attributes in increased detail (e.g. intersection or bottleneck effects). Moreover, the rising number of electric vehicles in the fleet during the recent years is a parameter that should be included in the aggregated emission factor estimation.

D7.10 New measurement and modelling methodologies for high resolution monitoring of urban anthropogenic and biogenic CO_2 fluxes

Table 4 Statistics of aggregated seasonal flux differences (Diff.) and hourly metrics (RMSE: root-mean-square error, MAE: mean absolute error) between eddy covariance measured FC,obs and hourly source area aggregated modelled FC,model for each wind sector (W, E) of the two eddy covariance sites (BKLI, BAES). The statistics are given separately for winter (Oct – Apr) and summer (May – Sep) periods, weekdays (WD) and weekends (WE), and for the whole period. N states the number of data pairs.

	BKLI-E		BKLI-W		BAES-E		BAES-W	
	WD	WE	WD	WE	WD	WE	WD	WE
Winter								
Diff. (µmol CO$_2$ m^{-2} s^{-1})	-1.7	-2.6	1.9	3.1	-3.8	-2.6	0.3	2.7
Diff. (%)	-8.5	-20.7	22.4	45.7	-23.1	-22.2	1.2	20.9
RMSE (µmol CO$_2$ m^{-2} s^{-1})	10.9	8.9	7.9	7.1	9.5	8.2	10.6	9.1
MAE (µmol CO$_2$ m^{-2} s^{-1})	7.7	6.0	5.5	5.1	6.5	5.7	8.2	7.0
N	4709	1815	2735	1146	4568	1905	3023	1166
Summer								
Diff. (µmol CO$_2$ m^{-2} s^{-1})	-1.4	-1.0	0.3	1.6	1.8	2.8	0.5	3.6
Diff. (%)	-8.3	-12.0	3.6	32.7	18.9	62.0	2.4	37.0
RMSE (µmol CO$_2$ m^{-2} s^{-1})	10.5	8.4	7.9	5.6	6.5	6.3	8.6	7.4
MAE (µmol CO$_2$ m^{-2} s^{-1})	7.3	5.7	4.9	3.9	4.5	4.3	6.4	6.1
N	3187	1147	2650	1162	2037	750	2877	1118
All								
Diff. (µmol CO$_2$ m^{-2} s^{-1})	-2.2		1.5		-2.1		1.0	
Diff. (%)	-12.8		20.2		-15.6		5.2	
RMSE (µmol CO$_2$ m^{-2} s^{-1})	10.2		7.4		8.4		9.3	
MAE (µmol CO$_2$ m^{-2} s^{-1})	7.1		5.0		5.7		7.1	
N	10860		7693		9261		8184	

The diFUME model incorporates human respiration and the biogenic components in greater detail than other models. Nevertheless, several enhancements are possible to improve the human and biogenic emissions in the model, such as using more detailed datasets for population density dynamics (e.g. mobile phone data) and accounting for more urban-specific growing conditions in the biogenic models (e.g. N fertilization, temperature spatial variability, elevated CO$_2$). Specifically, the diFUME biogenic flux model assumes similar photosynthetic behaviour among different vegetation types and species across the study area, simplifying the extreme diversity which is expected in the urban environment. Variability in photosynthetic capacities is more pronounced between different vegetation types, with grasses being potentially more productive than trees during the growing season (Larcher, 2003). Additionally, there are other potential sources of error in the biogenic model, such as the satellite-based LAI estimation and the approximation of θ spatial variability which is based only on three station measurements and does not account for irrigation in private gardens.

5 Conclusions

This report demonstrates the use of high-resolution urban bottom-up CO$_2$ flux models, combined with local-scale CO$_2$ flux observations from urban flux towers, as an approach to investigate the spatiotemporal dynamics of urban CO$_2$ fluxes. Both models (SUEWS and diFUME) simulate the main local scale CO$_2$ flux components of an urban area, focussing mostly on building heating emissions, vehicle traffic, human respiration and biogenic CO$_2$ processes (respiration, photosynthesis). Industrial and commercial emissions, agricultural/farming, waste management or other types of emissions are not taken into account with appropriate detail in these models. The two models are applied to two different cities in terms of emissions and climate. A big share of the urban emissions in Basel (CH) come from

building heating during winter, whereas this is not true in Heraklion (GR), where the vehicle traffic emissions dominate the whole year round.

It is demonstrated that the models can fairly capture the spatiotemporal dynamics of the urban CO$_2$ fluxes but in order to achieve that, they need already a considerable amount of local knowledge and data for their calibration. Flux towers are proved to be a very important source of information to calibrate the models. With appropriate analysis, the tower observations can reveal the emission behaviour of the surrounding area and even recognize the main emission sources.

A common conclusion in both study cases in this report is that the models tend to underestimate the magnitudes of the actual fluxes. This could be a calibration problem, but it could also indicate that the models are always an oversimplification of the actual processes. Cities are complex systems with complex behaviours, there are also unknown and unaccounted CO$_2$ sources across the cities that the models do not take into account. Biogenic CO$_2$ sources tend to be underestimated and they can be more unpredictable than the anthropogenic sources.

There is always room from improvement on the level of calibration and sophistication of the urban flux models. Taking into account more dynamic data sources (e.g. TomTom data, mobile activity) will probably produce better representations of the spatiotemporal CO$_2$ flux behaviour. However, the need for direct evaluation and calibration will be always very important. Flux towers are an important part of urban CO$_2$ flux monitoring systems. It is beneficial to employ several towers across the city to several locations with different emission characteristics in order to gain more complete overview of the flux profiles across the landscape. Finally, the flux observations can be used in statistical inversion systems to optimise the bottom-up model estimations and get more realistic flux estimations in high spatial and temporal resolutions.

6   Acknowledgements

7   References

3D-Stadtmodell. (2021). *Grundbuch- und Vermessungsamt Amtliche Vermessung*. https://www.geocat.ch/geonetwork/srv/ger/md.viewer#/full_view/a7fcab8f-8b17-4559-a77b-ed9f1bef5e1a

Amtliche Vermessung Basel-Stadt. (2021). *Bau- und Verkehrsdepartement, Grundbuch- und Vermessungsamt Amtliche Vermessung*. https://www.geocat.ch/geonetwork/srv/ger/%0Amd.viewer#/full_view/769225cf-1b31-46c9-ac74-6f41aaf832f6

Batchvarova, E., & Gryning, S. E. (1991). Applied model for the growth of the daytime mixed layer. *Boundary-Layer Meteorology*, *56*(3), 261–274. https://doi.org/10.1007/BF00120423

Beschäftigte und Arbeitsstätten. (2021). *No Title*. https://www.basleratlas.ch/#c=home

Buck, A. L. (1981). New equations for computing vapour pressure and enhancement factor. *Journal of Applied Meteorology*, *20*(12). https://doi.org/10.1175/1520-0450(1981)020<1527:nefcvp>2.0.co;2

Chrysoulakis, N., Ludlow, D., Mitraka, Z., Somarakis, G., Khan, Z., Lauwaet, D., Hooyberghs, H., Feliu, E., Navarro, D., Feigenwinter, C., Holsten, A., Soukup, T., Dohr, M., Marconcini, M., & Holt Andersen, B. (2023). Copernicus for urban resilience in Europe. *Scientific Reports*, *13*(1), 1–16. https://doi.org/10.1038/s41598-023-43371-9

Energiestatistik Basel-Stadt. (2020). *No Title*. https://www.statistik.bs.ch/analysen-berichte/raum-umwelt/energiestatistik.html

Fan, S.-M., Wofsy, S. C., Bakwin, P. S., Jacob, D. J., & Fitzjarrald, D. R. (1990). Atmosphere-biosphere exchange of CO2 and O3 in the central Amazon forest. *Journal of Geophysical Research*, *95*(D10). https://doi.org/10.1029/jd095id10p16851

Foken, T., & Wichura, B. (1996). Tools for quality assessment of surface-based flux measurements. *Agricultural and Forest Meteorology*, *78*(1–2), 83–105. https://doi.org/10.1016/0168-1923(95)02248-1

Gash, J. H. C., & Culf, A. D. (1996). Applying a linear detrend to eddy correlation data in realtime. *Boundary-Layer Meteorology*, *79*(3), 301–306. https://doi.org/10.1007/BF00119443

Gebäudeadressen und -informationen. (2022). *Bau- und Verkehrsdepartement, Grundbuchund Vermessungsamt Fachstelle für Geoinformation*. https://www.geocat.ch/%0Ageonetwork/srv/ger/md.viewer#/full_view/52a35a63-b873-48ce-800b-b5624f1da3e7

GMES/Copernicus land monitoring services. (2018). *Urban Atlas Land Cover/Land Use 2018 (vector), Europe, 6-yearly*. https://land.copernicus.eu/en/products/urban-atlas/urban-atlas-2018

Göckede, M., Foken, T., Aubinet, M., Aurela, M., Banza, J., Bernhofer, C., Bonnefond, J. M., Brunet, Y., Carrara, A., Clement, R., Dellwik, E., Elbers, J., Eugster, W., Fuhrer, J., Granier, A., Grünwald, T., Heinesch, B., Janssens, I. A., Knohl, A., … Yakir, D. (2008). Quality control of CarboEurope flux data - Part 1: Coupling footprint analyses with flux data quality assessment to evaluate sites in forest ecosystems. *Biogeosciences*, *5*(2), 433–450. https://doi.org/10.5194/bg-5-433-2008

Grimmond, C. S. B., Oke, T. R., & Steyn, D. G. (1986). Urban Water Balance: 1. A Model for Daily Totals. *Water Resources Research*, *22*(10), 1397–1403. https://doi.org/10.1029/WR022i010p01397

Hagolle, O., Huc, M., Desjardins, C., Auer, S., & Richter, R. (2017). *MAJA Algorithm Theoretical Basis Document. CNES, CESBIO & DLR Report ref MAJA-TN-WP2-030 Issue 1.0*. https://doi.org/10.5281/zenodo.1209633

HBEFA 4.1. (2021). *No Title*. https://www.hbefa.net/e/documents/HBEFA41_Development_Report.pdf

Järvi, L., Grimmond, C. S. B., & Christen, A. (2011). The Surface Urban Energy and Water Balance Scheme (SUEWS): Evaluation in Los Angeles and Vancouver. *Journal of Hydrology*, *411*(3–4), 219–237. https://doi.org/10.1016/j.jhydrol.2011.10.001

Järvi, Leena, Havu, M., Ward, H. C., Bellucco, V., McFadden, J. P., Toivonen, T., Heikinheimo, V., Kolari, P., Riikonen, A., & Grimmond, C. S. B. (2019). Spatial Modeling of Local-Scale Biogenic and Anthropogenic Carbon Dioxide Emissions in Helsinki. *Journal of Geophysical Research: Atmospheres*, *124*(15), 8363–8384. https://doi.org/10.1029/2018JD029576

Kaimal, J. C., & Finnigan, J. J. (1994). *Atmospheric boundary layer flows: their structure and measurement*. Oxford university press.

https://scholar.google.com/scholar_lookup?title=Atmospheric Boundary Layer Flows%3A Their Structure and Measurement&author=J.C. Kaimal&publication_year=1994

Kanda, M., Inagaki, A., Miyamoto, T., Gryschka, M., & Raasch, S. (2013). A New Aerodynamic Parametrization for Real Urban Surfaces. *Boundary-Layer Meteorology*, *148*(2), 357–377. https://doi.org/10.1007/s10546-013-9818-x

Kantonaler Richtplan Teilrichtplan Energie. (2020). *No Title*. https://www.aue.bs.ch/energie/gebaeude-energie/energierichtplan.html

Kljun, N., Calanca, P., Rotach, M. W., & Schmid, H. P. (2015). A simple two-dimensional parameterisation for Flux Footprint Prediction (FFP). *Geoscientific Model Development*, *8*(11), 3695–3713. https://doi.org/10.5194/gmd-8-3695-2015

Larcher, W. (2003). *Physiological plant ecology: ecophysiology and stress physiology of functional groups*. Springer Science & Business Media. https://scholar.google.com/scholar_lookup?title=Physiological Plant Ecology%3A Ecophysiology and Stress Physiology of Functional Groups&author=W. Larcher&publication_year=2003#d=gs_cit&t=1698002125512&u=%2Fscholar%3Fq%3 Dinfo%3AiUQa95_h1jwJ%3Ascholar.googl

Lietzke, B., & Vogt, R. (2013). Variability of CO2 concentrations and fluxes in and above an urban street canyon. *Atmospheric Environment*, *74*, 60–72. https://doi.org/10.1016/j.atmosenv.2013.03.030

Lietzke, B., Vogt, R., Feigenwinter, C., & Parlow, E. (2015). On the controlling factors for the variability of carbon dioxide flux in a heterogeneous urban environment. *International Journal of Climatology*, *35*(13), 3921–3941. https://doi.org/10.1002/joc.4255

Lindberg, F., Grimmond, C. S. B., Gabey, A., Huang, B., Kent, C. W., Sun, T., Theeuwes, N. E., Järvi, L., Ward, H. C., Capel-Timms, I., Chang, Y., Jonsson, P., Krave, N., Liu, D., Meyer, D., Olofson, K. F. G., Tan, J., Wästberg, D., Xue, L., & Zhang, Z. (2018). Urban Multi-scale Environmental Predictor (UMEP): An integrated tool for city-based climate services. *Environmental Modelling and Software*, *99*, 70–87. https://doi.org/10.1016/j.envsoft.2017.09.020

MacKerron, D. K. L. (2005). Agrometeorology. Principles and Application of Climate Studies in Agriculture . By H. S. Mavi and G. J. Tupper. Binghamton, NY, USA: Haworth Press (2004), pp. 364, US $95.95. ISBN 1-56022-972-1 . In H. S. Mavi & G. J. Tupper (Eds.), *Experimental Agriculture* (Vol. 41, Issue 2, pp. 267–267). Haworth Press. https://doi.org/10.1017/s0014479704212613

Matese, A., Gioli, B., Vaccari, F. P., Zaldei, A., & Miglietta, F. (2009). Carbon dioxide emissions of the city center of Firenze, Italy: Measurement, evaluation, and source partitioning. *Journal of Applied Meteorology and Climatology*, *48*(9), 1940–1947. https://doi.org/10.1175/2009JAMC1945.1

Mauder, M. & Foken, T. (2004). *Documentation and instruction manual of the eddy covariance software package TK2*. https://epub.uni-bayreuth.de/884/1/ARBERG026.pdf

McNorton, J., Agustí-Panareda, A., Arduini, G., Balsamo, G., Bousserez, N., Boussetta, S., Chericoni, M., Choulga, M., Engelen, R., & Guevara, M. (2023). An Urban Scheme for the ECMWF Integrated Forecasting System: Global Forecasts and Residential CO2 Emissions. *Journal of Advances in Modeling Earth Systems*, *15*(3), 1–18. https://doi.org/10.1029/2022MS003286

Moncrieff, J. B., J.M. Massheder, H. de Bruin, J. Elbers, T. Friborg, B. Heusinkveld, P. Kabat, S. Scott, H. Soegaard, & Verhoef, A. (1997). A system to measure surface fluxes of

momentum, sensible heat, water vapour and carbon dioxide. *Journal of Hydrology, 188–189*(1–4), 589–611. https://doi.org/10.1016/S0022-1694(96)03194-0

Moncrieff, J., Clement, R., Finnigan, J., & Meyers, T. (2004). Averaging, Detrending, and Filtering of Eddy Covariance Time Series. In X. Lee, W. Massman, & B. Law (Eds.), *Handbook of Micrometeorology* (pp. 7–31). Kluwer Academic Publishers. https://doi.org/10.1007/1-4020-2265-4_2

Nieuwstadt, F. T. M. (1981). The steady-state height and resistance laws of the nocturnal boundary layer: Theory compared with cabauw observations. *Boundary-Layer Meteorology, 20*(1), 3–17. https://doi.org/10.1007/BF00119920

Oke, T. R. (1987). *Boundary Layer Climates.* Routledge. https://doi.org/10.4324/9780203407219

Panagiotakis, E., Kolokotsa, D., & Chrysoulakis, N. (2021). Evaluation of nature-based solutions implementation scenarios, using urban surface modelling. In *Green Energy and Sustainability*. https://doi.org/10.47248/hkod902101010003

Salgueiro, V., Cerqueira, M., Monteiro, A., Alves, C., Rafael, S., Borrego, C., & Pio, C. (2020). Annual and seasonal variability of greenhouse gases fluxes over coastal urban and suburban areas in Portugal: Measurements and source partitioning. *Atmospheric Environment, 223*(December 2019). https://doi.org/10.1016/j.atmosenv.2019.117204

Schmutz, M., Vogt, R., Feigenwinter, C., & Parlow, E. (2016). Ten years of eddy covariance measurements in Basel, Switzerland: Seasonal and interannual variabilities of urban CO2 mole fraction and flux. *Journal of Geophysical Research, 121*(14), 8649–8667. https://doi.org/10.1002/2016JD025063

Stagakis, S., Chrysoulakis, N., Spyridakis, N., Feigenwinter, C., & Vogt, R. (2019). Eddy Covariance measurements and source partitioning of CO2 emissions in an urban environment: Application for Heraklion, Greece. *Atmospheric Environment, 201*(August 2018), 278–292. https://doi.org/10.1016/j.atmosenv.2019.01.009

Stagakis, S., Feigenwinter, C., Vogt, R., Brunner, D., & Kalberer, M. (2023). A high-resolution monitoring approach of urban CO2 fluxes. Part 2 - surface flux optimisation using eddy covariance observations. *The Science of the Total Environment, 903*(July), 166035. https://doi.org/10.1016/j.scitotenv.2023.166035

Stagakis, S., Feigenwinter, C., Vogt, R., & Kalberer, M. (2023). A high-resolution monitoring approach of urban CO2 fluxes. Part 1 - bottom-up model development. *Science of The Total Environment, 858*(July 2022), 160216. https://doi.org/10.1016/j.scitotenv.2022.160216

Stagakis, S., Markos, N., Vanikiotis, T., Tzotsos, A., Sykioti, O., & Kyparissis, A. (2015). SCASE: A primary productivity monitoring system for the forests of north pindus national park (epirus, greece). *European Journal of Remote Sensing, 48*, 223–243. https://doi.org/10.5721/EuJRS20154813

Strassen Wege. (2022). *Amt für Mobilität Mobilitätsstrategie.* https://www.geocat.ch/%0Ageonetwork/srv/ger/md.viewer#/full_view/1854ab2e-7a1d-4a93-bc67-95add757f283

Terrainmodell - DTM. (2022). *Grundbuch- und Vermessungsamt Amtliche Vermessung.* https://www.geocat.ch/geonetwork/srv/ger/md.viewer#/full_view/1bf94825-bd03-%0A41a6-aefb-3dbe79fd0689.

Verkehrsberuhigte Zonen. (2022). *Amt für Mobilität Mobilitätsstrategie.* https://www.geocat.ch/geonetwork/srv/ger/md.viewer#/full_view/9439aada-9c8a-4587-

a1deb0125b62a41f

Verkehrszähldaten. (2022). *No Title*. https://www.geocat.ch/geonetwork/srv/ger/md.viewer#/full_view/1631735b-e445-4d14-9121-92cdbf2764e3

Verkehrszähldaten motorisierter Individualverkehr. (2022). *Verkehrszähldaten motorisierter Individualverkehr*. https://www.mobilitaet.bs.ch/gesamtverkehr/verkehrskennzahlen/verkehrszaehlung.html

Vickers, D., & Mahrt, L. (1997). Quality control and flux sampling problems for tower and aircraft data. *Journal of Atmospheric and Oceanic Technology*, *14*(3), 512–526. https://doi.org/10.1175/1520-0426(1997)014<0512:QCAFSP>2.0.CO;2

Ward, H. C., Kotthaus, S., Järvi, L., & Grimmond, C. S. B. (2016). Surface Urban Energy and Water Balance Scheme (SUEWS): Development and evaluation at two UK sites. *Urban Climate*, *18*, 1–32. https://doi.org/10.1016/j.uclim.2016.05.001

Webb, E. K., Pearman, G. I., & Leuning, R. (1980). Correction of flux measurements for density effects due to heat and water vapour transfer. *Quarterly Journal of the Royal Meteorological Society*, *106*(447), 85–100. https://doi.org/10.1002/qj.49710644707

Wohnbevölkerung. (2021). *No Title*. https://www.basleratlas.ch/#c=home

Xie, Z. T., Coceal, O., & Castro, I. P. (2008). Large-Eddy simulation of flows over random urban-like obstacles. *Boundary-Layer Meteorology*, *129*(1), 1–23. https://doi.org/10.1007/s10546-008-9290-1

Zheng, Y., Havu, M., Liu, H., Cheng, X., Wen, Y., Lee, H. S., Ahongshangbam, J., & Järvi, L. (2023). Simulating heat and CO2 fluxes in Beijing using SUEWS V2020b: sensitivity to vegetation phenology and maximum conductance. *Geoscientific Model Development*, *16*(15), 4551–4579. https://doi.org/10.5194/gmd-16-4551-2023

Zilitinkevich, S. S., Tyuryakov, S. A., Troitskaya, Y. I., & Mareev, E. A. (2012). Theoretical models of the height of the atmospheric boundary layer and turbulent entrainment at its upper boundary. *Izvestiya - Atmospheric and Ocean Physics*, *48*(1), 133–142. https://doi.org/10.1134/S0001433812010148

Document History

Version	Author(s)	Date	Changes
0.1	FORTH	22/10/2023	First version
0.2	FORTH	16/11/2023	Final version

Internal Review History

Internal Reviewers	Date	Comments
Robbie Andrew (CICERO)	31/10/2023	
Marc Guevara Vilardell (BSC)	02/11/2023	
Stavros Stagakis (FORTH)	31/10/2023	

Estimated Effort Contribution per Partner

Partner	Effort
FORTH	3
Total	3

D7.10 New measurement and modelling methodologies for high resolution monitoring of urban anthropogenic and biogenic CO$_2$ fluxes